

Comparing gravitational redshifts of SDSS galaxy clusters with the magnification redshift enhancement of background BOSS galaxies

Pablo Jimeno^{1*}, Tom Broadhurst^{1,2}, Jean Coupon³, Keiichi Umetsu⁴, Ruth Lazkoz¹

¹ *Department of Theoretical Physics and History of Science, University of the Basque Country UPV-EHU, 48040 Bilbao, Spain*

² *IKERBASQUE, Basque Foundation for Science, Alameda Urquijo, 36-5 48008 Bilbao, Spain*

³ *Astronomical Observatory of the University of Geneva, ch. d'Ecogia 16, 1290 Versoix, Switzerland*

⁴ *Institute of Astronomy and Astrophysics, Academia Sinica, P.O. Box 23-141, Taipei 10617, Taiwan*

Draft version 19 November 2021

ABSTRACT

A clean measurement of the evolution of the galaxy cluster mass function can significantly improve our understanding of cosmology from the rapid growth of cluster masses below $z < 0.5$. Here we examine the consistency of cluster catalogues selected from the SDSS by applying two independent gravity-based methods using all available spectroscopic redshifts from the DR10 release. First, we detect a gravitational redshift related signal for 20,119 and 13,128 clusters with spectroscopic redshifts contained in the GMBCG and redMaPPer catalogues, respectively, at a level of $\sim -10 \text{ km s}^{-1}$. This we show is consistent with the magnitude expected using the richness-mass relations provided by the literature and after applying recently clarified relativistic and flux bias corrections. This signal is also consistent with the richest clusters in the larger catalogue of Wen et al. (2012), corresponding to $M_{200m} \gtrsim 2 \times 10^{14} M_{\odot} h^{-1}$, however we find no significant detection of gravitational redshift signal for less riched clusters, which may be related to bulk motions from substructure and spurious cluster detections. Second, we find all three catalogues generate mass-dependent levels of lensing magnification bias, which enhances the mean redshift of flux-selected background galaxies from the BOSS survey. The magnitude of this lensing effect is generally consistent with the corresponding richness-mass relations advocated for the surveys. We conclude that all catalogues comprise a high proportion of reliable clusters, and that the GMBCG and redMaPPer cluster finder algorithms favor more relaxed clusters with a meaningful gravitational redshift signal, as anticipated by the red-sequence colour selection of the GMBCG and redMaPPer samples.

Key words: cosmology: observations — dark matter — galaxies: clusters: general — gravitational lensing: weak

1 INTRODUCTION

The evolution of the mass function of galaxy clusters is sensitively related to cosmology via the dynamically opposing effects of gravity and the cosmological acceleration (see Huterer et al. (2013) for a thorough review). It has been claimed that with only a few hundred massive clusters below redshift $z \sim 0.5$, competitive constraints on the standard cosmological model and a consistency check of the viability of general relativity on cluster scales can be achieved (Allen et al. 2004; Mantz et al. 2014; Rapetti et al. 2013). In terms of the standard model the parameters most sensitively

constrained are the normalization of the mass function, σ_8 , and the cosmological mean matter density, Ω_M . These parameters can in principle be constrained using the most massive clusters (Harrison & Coles 2012; Waizmann et al. 2011; Watson et al. 2014). Currently the samples of clusters constructed for these purposes are X-ray or Sunyaev-Zel'dovich (SZ) effect selected so that the masses are generally inferred from indirect scalings derived from other samples of clusters at lower redshift related to lensing and/or internal dynamics. Efforts are underway to obtain accurate masses of sizable samples of massive clusters from deep multi-band lensing observations, such as the CLASH survey (Umetsu et al. 2014; Merten et al. 2014) and the “Weighing the Giants” project (von der Linden et al. 2014). These samples are a

* E-mail: pablodavid.jimeno@ehu.es

substantial step forward in that lensing based masses are constructed but they still rely on X-ray selection, with a significant scatter and the potential for serious biases when inferring masses indirectly this way (Rozo et al. 2009a). Ideally the sample selection would be best made by selecting clusters in a volume limited way from densely sampled redshift surveys with masses obtained by weak lensing. Large surveys with the resolution for weak lensing work are underway: HSC (Takada 2010), JPAS (Benitez 2014) and planned eBOSS, Large Synoptic Survey Telescope (LSST), EUCLID, Wide-Field Infrared Survey Telescope (WFIRST), and the Dark Energy Survey (DES), but currently no statistical sample of clusters selected this way exists.

The relation between richness and mass has been shown to be fraught with systematic uncertainty (Rozo et al. 2009a) related perhaps mainly to the complexities of gas physics that may be expected to significantly complicate the conversion of X-ray or SZ luminosities to total cluster mass. Weak lensing mass measurements for subsamples of relaxed clusters can help reduce the scatter in mass-observable scaling relations (von der Linden et al. 2014). Recent cluster weak lensing efforts with deep Subaru observations have achieved an accuracy of sub-10% in the overall cluster mass calibration (von der Linden et al. 2014; Umetsu et al. 2014), which is currently limited by relatively small sample sizes.

While we await the new lensing surveys, we can examine the new optically selected samples of clusters constructed from the huge volume observed by the SDSS and BOSS surveys for which many tens of thousands of clusters have been painstakingly identified independently by several groups using different cluster finding algorithms.

Among some of the recent ones, based on SDSS data, we find the maxBCG catalogue (Koester et al. 2007), which is based on red-sequence cluster detection techniques and provided 13,823 clusters with photometric redshifts (hereafter photo- z 's) using SDSS DR5 data. Szabo et al. (2011), using an adaptive matched filter (AMF) cluster finder (Dong et al. 2008), presented an optical catalogue of 69,173 clusters in the redshift range $0.045 \leq z < 0.78$, based on SDSS DR6 data. This catalog, differing from others, did not rely on the presence of a luminous central galaxy in order to detect and measure the properties of the cluster, but provided a catalogue with the three brightest galaxies associated to them. Using also DR6 photometric data, Wen et al. (2009) found 39,716 clusters of galaxies below redshift $z = 0.6$, identifying as clusters those groups with more than eight $M_r \leq -21$ galaxies inside a determined volume. Tempel et al. (2014) construct flux- and volume-limited galaxy groups catalogues from SDSS spectroscopic data using a variable linking length friends-of-friends (FoF) algorithm. The masses of the groups are estimated using the velocity dispersion measurements via the virial theorem, and although 82,458 groups are found, only around 2,000 of them have masses above $10^{14} M_{\odot}$. The CAMIRA algorithm by Oguri (2014), based on colour prediction of red-sequence galaxies in clusters, provides richness and photometric redshift estimates for 71,743 clusters in the $0.1 < z < 0.6$ redshift range using SDSS DR8 photometric data.

Using three of the largest cluster catalogues produced to date, and described in the next section, we relate the optical richness to statistical measures of mass related observables,

in particular we focus here on the effects of gravitational redshift and gravitational magnification.

The effect of gravitational redshift is simply a consequence of the reduced frequency of light observed for objects emitting from a lower gravitational potential relative to the observer. This relativistic effect has been advocated in terms of the change in frequency of emission lines present in the hot cluster gas (Broadhurst & Scannapieco 2000) which may be applied to individual relaxed clusters where bulk gas motions do not dominate. This new observational signature of clusters differs from others, in the sense that it provides a novel and unique way to test gravity, as modified gravity could lead to deeper potential wells inside clusters, and thus, stronger gravitational redshift than the one predicted by general relativity (Gronke et al. 2014; Jain et al. 2013). A statistical effect on the redshifts of member galaxies has been claimed to be detected for optically selected stacked cluster samples from the SDSS survey (Wojtak et al. 2011; Domínguez Romero et al. 2012; Sadeh et al. 2014), for which the brightest cluster galaxy (BCG) is found to lie systematically offset in velocity relative to other member galaxies.

The sense of this effect is opposite to that induced by tangential motion (Zhao et al. 2013) and other effects related to galaxy kinematics (Kaiser 2013). All these effects combined induce a new asymmetry on the cross-correlation function (Croft 2013; Bonvin et al. 2014), different from the well known redshift-space distortion asymmetry, as it depends not only on the absolute value of the line-of-sight separation from the center of the cluster, but also on its sign.

The magnification bias effect that we explore here is related to the increased flux from background galaxies, which promotes galaxies above the flux limit whilst magnifying the area of sky over which they are detected, leading to greater depth for luminous background galaxies (Broadhurst, Taylor & Peacock 1995). A significant detection of this redshift enhancement effect has been reported recently by Coupon et al. (2013, hereafter, CBU13) combining SDSS clusters and lensing background galaxies from the BOSS survey. Here we explore this effect further with the new data releases in an enlarged sample of clusters and background galaxies, allowing new correlations to be examined in this context. This effect has the advantage over weak lensing estimated from shear to be free from the large intrinsic and instrumental shape dispersion. It requires on the other hand a clean sample of background galaxies with accurate spectroscopic redshifts, limited to fewer galaxies.

Individual massive clusters now routinely provide a measurement of magnification bias, in terms of the background counts. This effect is a projection over the integrated luminosity function described above, which it has been shown reduces significantly the surface number density of red background galaxies behind individual clusters (Broadhurst et al. 2005; Umetsu et al. 2011, 2012; Umetsu 2013) and similar effects are claimed for background QSO's and Lyman break galaxies (Ford et al. 2012; Hildebrandt et al. 2013). The expansion of the sky by magnification is found to dominate over the opposing increase from objects promoted from lower luminosity above the flux limit. The requirement for this is deep imaging (Umetsu et al. 2014; Taylor et al. 1998), so that this effect can be traced with sufficient numbers over several inde-

pendent radial bins per cluster. Umetsu et al. (2011) have shown that this effect can significantly enhance the accuracy of lensing derived cluster masses when added to weak shear measurements.

In this study we provide these two independent gravitational measurements for the three large stacked samples of SDSS clusters described in section 2. In section 3 we define the phase-space region in which we will measure the velocity distribution of galaxies around clusters to identify any possible gravitational redshift or internal motion related effects. For the magnification we examine the mean redshift of background BOSS galaxies in section 4 and report our conclusion in section 5. Throughout this paper we adopt the standard cosmological parameters of a fiducial flat Λ CDM cosmology (Komatsu et al. 2011) with $H_0 = 72 \text{ km s}^{-1} \text{ Mpc}$ and $\Omega_m = 0.26$. To quantify cluster masses we adopt M_{200m} units, i.e., mass measured with respect to 200 times the *mean* background density of the universe. We use the prescription given by Hu & Kravtsov (2003) to convert between different mass definitions, which assumes a Navarro-Frenk-White (Navarro et al. 1997, hereafter NFW) halo density profile, using the concentration-mass relations provided by Bhattacharya et al. (2013).

2 DATA

We use the data from the Sloan Digital Sky Survey (SDSS), a combined photometric and spectroscopic survey conducted on a 2.5-meter wide angle telescope located at Apache Point Observatory (Gunn et al. 2006). The SDSS covers a unique footprint of $14,555 \text{ deg}^2$ of sky, and comprises optical imaging data of nearly 500 million unique objects in five filters (u, g, r, i and z) and over 1,600,000 unique spectra obtained with the original SDSS spectrograph (640 spectroscopic fibers per plate) under the Legacy programme. The ongoing BOSS programme aims at complementing the spectroscopic sample with a total of 1,400,000 color-selected galaxies in the range $0.3 < z < 0.7$ with the newly installed BOSS spectrograph (1,000 fibers per plate, Smee et al. 2013). Here we use the DR10 release which contains all galaxies with reliable spectroscopic measurements from the Legacy programme plus more than 850,000 galaxies from the BOSS programme.

2.1 SDSS Cluster Catalogues

Large numbers of clusters with spectroscopic redshift measurements are needed to statistically investigate their gravitational redshift and lensing properties, so here we will focus our study on the three catalogues described below, which offer the largest samples useful for us to date. Throughout this paper we convert the richness observable into mass for comparison purposes, using the richness-mass relations appropriate for each case. The sky, redshift and mass distributions of these resulting cluster samples and their mass distributions are shown in Figs. 1, 2, and 3. We summarize the cluster samples properties in Table 1, where the final number of clusters considered in this study, N_{clusters} , takes into account the restrictions applied in Sec. 3.

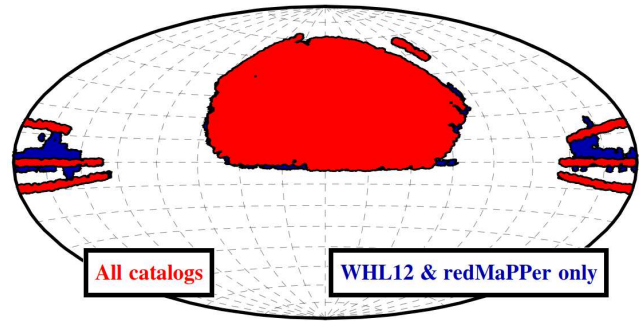


Figure 1. Clusters distribution on the sky, using equal-area map projection. We are considering here the final sample of clusters that we will be using in our study, that is, those with good spectroscopic measurements of the central BCG. This leaves a final sample of 20,119 for the GMBCG catalogue case, 52,682 for the WHL12 catalogue, and 13,128 for the redMaPPer cluster catalogue. After the restrictions applied in Sec. 3, these samples are reduced to 4,278, 12,661 and 3,372 clusters, respectively.

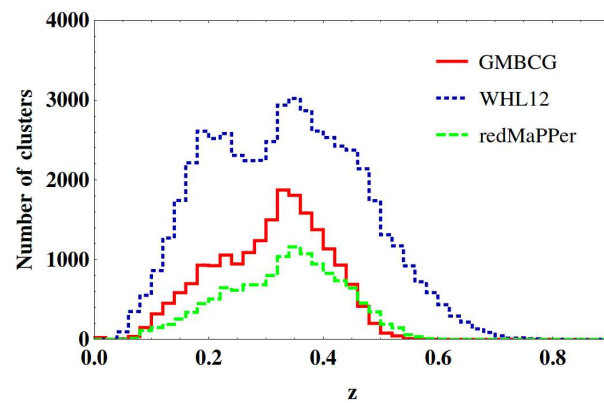


Figure 2. GMBCG (dotted, red), WHL12 (continuous, blue) and redMaPPer (dashed, green) cluster redshift distributions.

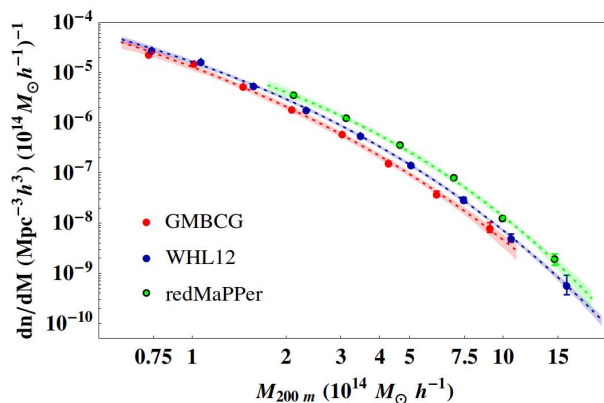


Figure 3. Observed mass distributions of clusters. Here dn/dM is the differential number of clusters per unit of comoving volume and unit of mass. In order to model this mass distribution, for each cluster sample we fitted a functional mass function, shown as the dotted lines, which spans from the least massive cluster contained in each catalogue, to the most massive one. The shaded regions represent 90% confidence range.

Catalogue	N_{clusters}	$\langle z \rangle$	$\langle M_{200m} \rangle [10^{14} M_{\odot} h^{-1}]$	Ref.
GMBCG	4,278	0.22	1.5	(1)
WHL12	12,661	0.19	1.4	(2)
redMaPPer	3,372	0.23	3.2	(3)

Table 1. Properties of the cluster samples considered. References: (1): Hao et al. (2010), (2): Wen et al. (2012), (3): Rykoff et al. (2014).

2.1.1 GMBCG Cluster Catalogue

We use the optical-based cluster catalogue presented by Hao et al. (2010), obtained applying the ‘‘Gaussian Mixture Brightest Cluster Galaxy’’ (GMBCG) algorithm to the SDSS DR7 data. This cluster finding algorithm relies on the galaxy red sequence pattern and the presence of a BCG as key features of galaxy clusters. The SDSS photometric and redshift catalogues are used to determine BCG candidates. To estimate the richness R of the cluster, a combination of Gaussian fitters in colour space is used to identify overdensities around a BCG candidate among galaxies brighter than $0.4L^*$ (see Blanton et al. 2003), closer than 0.5 Mpc from the BCG, and within a photo- z range of ± 0.25 . Then a circular aperture scaled to the amplitude of the overdensity around the BCG is set to recompute the richness of the cluster. Only clusters with $R \geq 8$ are included in the final catalogue. The resulting sample created from the application of this method comprises 55,424 clusters, and is approximately volume limited up to redshift $z \sim 0.4$, showing high purity and completeness in this range. Of all these clusters we will be interested in 20,119 of them, which have spectroscopic redshift measurements of their associated BCGs. We will refer to this sample of clusters as the ‘‘GMBCG’’ catalogue.

We use the richness-mass relation provided by the authors of the maxBCG catalogue (Rozo et al. 2009a, 2009b), which uses the same richness definition as the GMBCG catalogue:

$$M_{500c} = \exp(0.62) \left(\frac{R}{40} \right)^{1.06} \times 10^{14} M_{\odot} h^{-1}, \quad (1)$$

where R accounts for the richness estimation provided by the catalog, and M_{500c} is the cluster mass contained within the radius r_{500c} , where the mean density of the cluster is 500 times the *critical* density of the universe at the redshift of the cluster. We then convert M_{500c} into M_{200m} . Finally, we would like to clarify that we will be working with the richness measurement recommended by the catalogue authors, that is, `GM_Ngals_weighted` instead of `GM_Scaled_Ngals` when `WeightOK` is set equal to 1.

2.1.2 WHL12 Cluster Catalogue

Using photometric redshifts, Wen et al. (2012) have identified 132,684 clusters from SDSS DR8 below redshift $z \sim 0.8$. A FoF algorithm links galaxies closer than 0.5 Mpc in the transverse direction and with a photo- z value differing less than $\pm 0.04(1+z)$. When an overdensity is detected, the galaxy with the maximum number of links to other cluster candidates is taken as a temporary center, and the BCG is identified as the brightest among those galaxies closer than a linking length from this temporary center. Then, the to-

tal luminosity of the cluster candidate in the r -band is calculated as the sum of all those members with luminosities brighter than $0.4L^*$, and used to estimate its richness R_{L^*} . A galaxy cluster is included in the catalogue if $R_{L^*} \geq 12$. Because of the magnitude limit of the SDSS photometric data, this catalogue is claimed to be complete up to redshift $z \sim 0.42$ to a 95% level, in the sense that there are almost no missing members among the galaxies contributing to the estimation of the cluster richness. Among these 132,684 clusters, 52,682 of them have spectroscopic redshifts of the BCGs, obtained from SDSS DR9, and lie within the region of interest for us. As we can see from Fig. 2, WHL12 is the catalogue that provides the largest sample of clusters in all redshift ranges. From now on, this catalogue will be referred to as ‘‘WHL12’’.

We use the richness-mass relation provided by the authors of the catalog:

$$M_{200c} = 10^{-1.63} R^{1.17} \times 10^{14} M_{\odot} h^{-1}, \quad (2)$$

calibrated using X-ray and lensing data. We then convert M_{200c} into M_{200m} .

2.1.3 redMaPPer Cluster Catalogue

More recently, Rykoff et al. (2014) have presented a ‘‘red-sequence Matched-filter Probabilistic Percolation’’ (redMaPPer) cluster finding algorithm, prepared to process large amounts of photometric data. It may be considered as an improved version of the maxBCG and the GMBCG cluster finding algorithms, as the red-sequence cluster detection and the richness estimation process have been developed using the lessons obtained from these two previous catalogs. This algorithm makes use of spectroscopic data to self-train the red-sequence model that is used to find clusters within the data. The authors of this catalogue argue that their method outperforms photo- z algorithm finders in the redshift range where this catalogue is defined, although for higher redshifts these will perform better as the red-sequence clusters are of low contrast.

The richness estimator, λ , developed for this sample is based on the previous optical single-color richness estimator, λ_{col} , of Rozo et al. (2009a) and Rykoff et al. (2012), with several improvements to take into account things such as the survey mask, the probability of each galaxy to belong to the cluster, the contribution of foreground and background galaxies, etc. We refer the reader to Rykoff et al. (2014) for further details. In order to obtain a mass estimate from the richness provided by the catalog, we will use the richness-mass relation as provided in Rykoff et al. (2012):

$$M_{200m} = \exp(1.69) \left(\frac{\lambda_{\text{col}}}{60} \right)^{1.08} \times 10^{14} M_{\odot} h^{-1}. \quad (3)$$

Although the richness estimators λ_{col} and λ differ in many aspects, it is shown that the median deviation between them is no larger than 10%. It may be noted that this does not provide a rigorous mass calibration, as it is based on abundance matching techniques using a Tinker et al. (2008) mass function, and it has not been corrected for selection effects. A more precise richness-mass relation is announced to be released in the future by the authors. Meanwhile, for comparison purposes, we will make use of the current relation provided.

The redMaPPer algorithm has been applied to the SDSS DR8 photometric catalogue. In order to provide a robust cluster catalogue, a conservative cut of $\lambda/S(z) > 20$ (corresponding to $M_{200m} > 1.75 \times 10^{14} M_{\odot} h^{-1}$) is applied to the algorithm finder, where a scaling factor $S(z)$ is introduced to correct for the survey depth, so that for $z < 0.35$, $S(z) = 1$, and the number of galaxies observed is equal to λ , whereas it is equal to $\lambda/S(z)$ for $z \geq 0.35$. A total number of 25,236 clusters were obtained in the redshift range $0.08 \leq z \leq 0.55$. Of these, we will be using 13,128, which also have spectroscopic measurements of their BCG.

This catalogue is claimed to be volume-limited up to redshift $z \sim 0.35$ with a purity $> 95\%$, where purity in this case is defined in a way such that “impurities” represent richness measurements affected by projection effects. For $\lambda > 30$ and $z < 0.3$, the completeness is as high as $\gtrsim 99\%$.

2.2 SDSS spectroscopic samples

We have independently used the “Legacy” and “BOSS” spectroscopic samples in the SDSS to select the cluster galaxies needed to measure the gravitational redshift effect, and the background galaxies needed for the redshift enhancement, respectively.

The Legacy survey spectroscopic redshifts were obtained as part of the SDSS-I and SDSS-II programmes (York et al. 2000), over an observing period of eight years, shared with two additional surveys, the Sloan Extension for Galactic Understanding and Exploration (SEGUE, for stars) and a Supernova survey. The Legacy Survey, originally designed to investigate the large-scale structure of the universe is composed of:

- the *Main* sample (Strauss et al. 2002), a magnitude-limited sample of galaxies with r -band Petrosian magnitudes $r < 17.7$, and a median redshift of $z \sim 0.1$;
- and the *Luminous Red Galaxies* (LRG) sample (Eisenstein et al. 2001), an approximately volume-limited sample up to $z \sim 0.4$.

With a total sky coverage of $8,032 \text{ deg}^2$, as shown in Fig. 4, the Legacy Survey includes over 930,000 unique galaxies with a spectroscopic redshift. Of those, we select the most reliable spectra with flags `ZWARNING` equal to 0 or 16, `plateQuality` “good” or “marginal”, and `Z_ERR` < 0.0006 . Within the redshift range in common with the cluster catalogues listed in Sec. 2.1, we find 801,945 galaxy spectra useful for our purposes. Although the spectroscopic sample and sky coverage of the Legacy sample have remained unchanged, the imaging and the spectroscopic pipelines have been improved in subsequent SDSS data releases. Thus, here we use the Legacy survey spectra of the latest DR10 release (Ahn et al. 2014). The redshift distribution of this sample of galaxies is shown in Fig. 5. Most of these galaxies are confined in the range $0 < z < 0.2$, with an extra contribution coming from LRGs at higher redshift that peaks at $z \sim 0.35$.

The ongoing Baryon Oscillation Spectroscopic Survey (BOSS, Dawson et al. 2013) is part of the six-year SDSS-III programme Eisenstein et al. 2011, which aims to obtain the spectroscopic redshifts of 1.5 million luminous red galaxies out to $z = 0.7$, and the Lyman- α absorption lines of 160,000 quasars in the range $2.2 < z < 3$, to measure the acoustic scale with a precision of 1% at redshifts $z = 0.3$ and $z =$

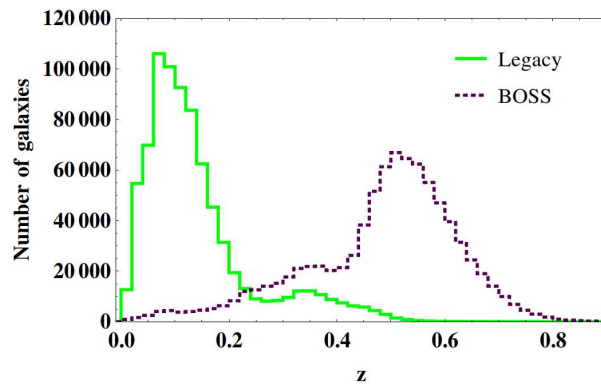


Figure 5. Legacy (continuous, green) and BOSS (dashed, purple) galaxy redshift distributions.

0.55. This latest publicly available set of data provides the spectra of 859,322 unique galaxies over $6,373 \text{ deg}^2$ (in green in Fig. 4). As we did with the Legacy spectra, we select only the most reliable galaxies, imposing `ZWARNING_NOQSO=0` to be 0, and removing objects with `plateQuality` set to “bad” or `Z_ERR_NOQSO > 0.0006`. This gives us a sample of 855,097 galaxies. As seen from the redshift distribution in Fig. 5, most of BOSS galaxies lie above $z \sim 0.4$.

3 GRAVITATIONAL REDSHIFT AND OTHER INTERNAL REDSHIFT EFFECTS

General relativistic time dilation means light emitted from within a gravitational potential is redshifted relative to a distant observer, in proportion to the potential depth in the weak field limit. This means we may expect centrally located BCG galaxies to be relatively more affected than the average cluster member (Broadhurst & Scannapieco 2000). This relative gravitational redshift (GR), Δz_{GR} , is proportional to $\Delta\Phi/c^2$, where $\Delta\Phi$ is the gravitational potential difference between the cluster galaxy and the cluster BCG. Wojtak et al. claimed in 2011 to have measured for the first time this effect, using the GMBCG cluster catalogue and DR7 data. Analytic models (Cappi 1995) predict a gravitational redshift of the order of $c\Delta z_{\text{GR}} \sim 10 \text{ km s}^{-1}$ for clusters with masses $\sim 10^{14} M_{\odot}$, consistent with Wojtak et al. measurements, and as much as 300 km s^{-1} for clusters with masses $\sim 10^{16} M_{\odot}$.

Making use of N-body simulations in a Λ CDM universe, Kim & Croft (2004) concluded that, assuming a redshift accuracy of 30 km s^{-1} , over 5,000 clusters with masses above $\sim 5 \times 10^{13} M_{\odot}$ were needed in order to measure the gravitational redshift effect at the 2σ level. An important result of their study is that, above masses $\sim 10^{14} M_{\odot}$, the gravitational redshift signal is proportional to the cluster velocity dispersion, and hence, the number of clusters actually needed to detect the gravitational redshift signal does not depend on the mass of the clusters used. This is because the dispersion in the velocity difference between the BCG and the rest of the galaxies is found to increase with cluster mass in the simulations, adding to the inherent noise. They stress that a convincing detection would require sufficient data so that independent mass bins can be compared to ex-

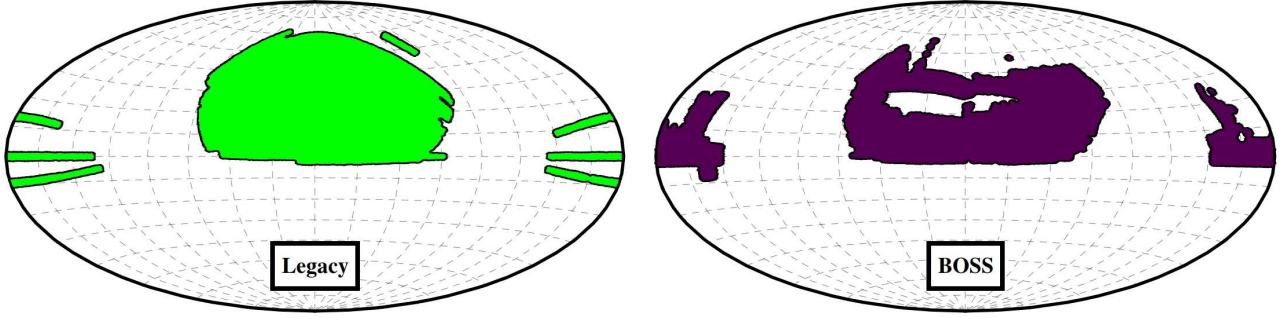


Figure 4. Legacy (left) and BOSS (right) galaxies sky distributions, as available in DR10. In this study we use 801,945 galaxy spectra in the Legacy survey and 855,097 in the BOSS survey.

amine the signature of gravitational redshift as a function of cluster mass.

Shortly after the Wojtak et al. claim, Zhao et al. (2013) pointed out a potentially significant additional new blueshift deviation effect related to the special relativistic transverse doppler effect (TD) generated by random motion of the galaxies moving within the cluster potential. This additional shift Δz_{TD} is equal to $(\langle |\mathbf{v}_{\text{gal}}|^2 \rangle - |\mathbf{v}_{\text{BCG}}|^2)/2c^2$, opposite in sign to the GR shift, and of the same order of magnitude for clusters in virial equilibrium. In fact, for a spherical cluster in equilibrium, this yields $c \Delta z_{\text{TD}} = (3\sigma_{\text{obs}}^2 - 3\sigma_{\text{BCG}}^2)/2c$, where σ_{obs} is the observed line-of-sight velocity dispersion of the galaxies around the BCG, and σ_{BCG} is the velocity dispersion associated to BCGs, which is taken to be $\sigma_{\text{BCG}} \sim \sigma_{\text{obs}}/3$ by Wojtak et al. and Zhao et al.

More recently, Kaiser (2013) has raised other significant corrections. As we are observing galaxies in our past light cone (LC), and due to the time it takes light to travel through the cluster, we will see on average more galaxies moving away from us than toward us. This effect is compared by Kaiser to the one that “causes a runner on a trail to meet more hikers coming toward her than going in the same direction”. This results in another shift of the distribution of galaxies around the BCGs equal to $c \Delta z_{\text{LC}} = (\langle |\mathbf{v}_{\text{los gal}}|^2 \rangle - |\mathbf{v}_{\text{los BCG}}|^2)/c$, equal in sign to the TD effect, and of the same order of magnitude.

In addition to that, according to Kaiser we also have to deal with the fact that we are working with a magnitude-limited sample of galaxies: although the cluster catalogues, that are obtained using photometric data, are claimed to be volume complete up to a certain redshift limit $z \sim 0.4$, the sample of galaxies with measured redshifts is usually magnitude-limited, so that proper motion, changing the surface brightness (SB), or equivalently the apparent luminosity of galaxies due to the relativistic beaming effect, will bias the distribution of galaxies selected within clusters. For low velocities, this change in the luminosity is equal to $\Delta L/L = (3 + \alpha(z)) v_{\text{los}}/c$, with L the apparent luminosity of the galaxy, and $\alpha(z)$ the effective spectral index that takes into account the change in frequency and the resulting response of the photon count detector to this change.

The modulation on the number of observable galaxies is thus obtained multiplying $\Delta L/L$ by the logarithmic derivative of the comoving density of observable objects n_{obs} above the luminosity limit $L_{\text{lim}}(z)$, $d \ln n_{\text{obs}}[> L_{\text{lim}}(z)]/d \ln L$, which depends on the redshift

distribution and the luminosity function associated to the galaxy survey considered, and its average on the redshift limits considered. This density modulation introduces a change on the observed distribution of galaxies equal to $c \Delta z_{\text{SB}} = -\langle (3 + \alpha(z)) d \ln n/d \ln L \rangle \langle |\mathbf{v}_{\text{los}}|^2 \rangle / c$. In opposition to the others TD and LC dynamical effects, this new shift introduces a net blue-shift, also of the same order of magnitude.

Hence, the total redshift velocity difference v_{los} between a galaxy and the central BCG is given by:

$$v_{\text{los}} = H(z) (d_{\text{gal}} - d_{\text{BCG}}) + v_{\text{pec}} + c \Delta z, \quad (4)$$

where $H(z)$ is the Hubble parameter, d is the distance between the observer and the object in Mpc, v_{pec} is the velocity due to the peculiar motion of the galaxy, and Δz is the term arising from the combination of the previously mentioned distortions. From now on, we will refer to the combination of all these effects as an “internal redshift”.

3.1 Model

We compute now the expected internal redshift, Δz , coming from the previously mentioned gravitational redshift (GR), transverse doppler (TD), past light cone (LC) and surface brightness (SB) effects for GMBCG, WHL12 and redMaPPer catalogues. The internal redshift that one would observe at a projected transverse distance r_{\perp} from the center of a cluster halo with mass M would be:

$$\Delta z = \Delta z_{\text{GR}} + \Delta z_{\text{TD}} + \Delta z_{\text{LC}} + \Delta z_{\text{SB}}, \quad (5)$$

with:

$$\Delta z_{\text{GR}} = \frac{-2}{c^2 \Sigma(r_{\perp})} \int_{r_{\perp}}^{\infty} \Delta \Phi(r) \frac{\rho_{\text{NFW}}(r) r dr}{\sqrt{r^2 - r_{\perp}^2}}, \quad (6)$$

$$\Delta z_{\text{TD}} = \frac{1}{2c^2} (\langle |\mathbf{v}_{\text{gal}}|^2 \rangle - |\mathbf{v}_{\text{BCG}}|^2), \quad (7)$$

$$\Delta z_{\text{LC}} = \frac{1}{c^2} (\langle |\mathbf{v}_{\text{los gal}}|^2 \rangle - |\mathbf{v}_{\text{los BCG}}|^2), \quad (8)$$

$$\Delta z_{\text{SB}} = \frac{-\langle |\mathbf{v}_{\text{los gal}}|^2 \rangle}{c^2} \langle (3 + \alpha(z)) \frac{d \ln n_{\text{obs}}[> L_{\text{lim}}(z)]}{d \ln L} \rangle, \quad (9)$$

where Σ is the projected surface density of the NFW density profile ρ_{NFW} of a cluster halo with mass M , and $\Delta \Phi(r)$ is the potential energy difference between r and the center of such halo. We use the prescription given by Zhao et al. to compute $\langle |\mathbf{v}_{\text{gal}}|^2 \rangle$ as a function of the potential via the isotropic Jeans equation:

$$\langle |\mathbf{v}_{\text{gal}}|^2 \rangle = 3 \sigma_{\text{los}}^2 = 3 \left\langle \sqrt{r^2 - r_{\perp}^2} \frac{\partial \Phi}{\partial (\sqrt{r^2 - r_{\perp}^2})} \right\rangle. \quad (10)$$

The value of $\alpha(z)$ can be taken to be approximately 2, and, to compute $d \ln n / d \ln L$, we take $r < 17.77$ as the apparent magnitude limit for our galaxies sample, and use the estimate of the luminosity function in the $0.1r$ -band given by Montero & Prada (2009) based on DR6 data, whose Schechter best fit parameters are: $\Phi_* = 0.0093$, $M_* - 5 \log_{10} h = -20.71$ and $\alpha = -1.26$. It would be more accurate to use the specific luminosity function associated to galaxies belonging to the clusters considered, but it was shown by Hansen et al. (2009) that it doesn't differ much from the overall survey luminosity function, so we can use it as a good approximation. To calculate the average we use the Legacy galaxy distribution seen in Fig. 5:

$$\langle d \ln n / d \ln L \rangle = \frac{\int_{z_1}^{z_2} (d \ln n / d \ln L) (dN/dz) dz}{\int_{z_1}^{z_2} (dN/dz) dz}, \quad (11)$$

where the lowest z_1 and highest z_2 redshift limits of integration are chosen according to the cluster sample considered in each case.

The velocity total shift observed from a stacked sample of cluster haloes would then be:

$$\Delta(r_{\perp}) = c \frac{\int_{M_1}^{M_2} \Delta z (M, r_{\perp}) \Sigma(r_{\perp}) (dn(M)/dM) dM}{\int_{M_1}^{M_2} \Sigma(r_{\perp}) (dn(M)/dM) dM} \quad (12)$$

where we integrate between the mass range defined by the lowest M_1 and highest M_2 masses considered in each catalog, and the mass distribution in each case is given by $dn(M)/dM$, which is functionally fitted from the observed distribution of clusters, as in Fig. 3, but in this case considering only those that were not discarded in the process, that is, with sufficient nearby galaxies with spectroscopic measurements for a meaningful measurement. The model curves predict almost the same internal redshift for both GMBCG and WHL12 cluster samples, as the lowest mass and the mass distribution of clusters are almost identical for both catalogues. The main difference between these two catalogues, i.e., WHL12 ranging to higher masses, does not change the shape of the model curve too much as the contribution coming from high mass clusters is highly suppressed by the low values of the mass function distribution at these scales. The redMaPPer model curve, in the other hand, predicts a higher signal, which is consistent with the fact that redMaPPer minimum mass cutoff is much more conservative than GMBCG and WHL12 ones, resulting in a higher average cluster mass.

3.2 Experimental Results

In order to study the spatial distribution of galaxies around clusters, first, we carefully remove the identified BCGs of the cluster catalogues from the SDSS galaxy catalogues. Here we take into account the fact that, according to SDSS specifications, two galaxies are considered as the same object if they are closer than 3 arcsecs in the Legacy Survey case, and 2 arcsecs in the BOSS Survey case. Also, this will help us identify which of the BCGs have the best spectroscopic measurements, so, taking a conservative approach, we will only work with those BCGs identified in our ‘‘high quality’’

SDSS galaxy sample, discarding this way BCG redshift measurements obtained from ‘‘bad’’ plates. This leaves us with a total sample of 19,867 BCGs in the GMBCG catalog, 52,255 in the WHL12 case, and 10,197 in the redMaPPer one. We compute the projected transverse distance r_{\perp} and the line-of-sight velocity $v_{\text{los}} = c(z_{\text{gal}} - z_{\text{BCG}})/(1 + z_{\text{BCG}})$ of all SDSS galaxies with respect to the BCGs, and keep those that lie within a separation of $r_{\perp} < 7$ Mpc and $|v_{\text{los}}| < 6,000 \text{ km s}^{-1}$ from these. It should be noted that, as we are working mainly in a low redshift region, the impact of the cosmological parameters used is not significant. Stacking all the obtained pairs into one single phase-space diagram, we get the density distributions shown on the left handside of Fig. 6.

To remove the contribution of foreground and background galaxies not gravitationally bound to clusters, we adopt an *indirect* approximation, where galaxies not belonging to clusters are not identified individually in each cluster, as in the *direct* method, but taken into account statistically once all the cluster information has been stacked into one single distribution of galaxies. See Wojtak et al. (2007) for a detailed study of different direct and indirect foreground and background galaxies removal techniques.

In our case, we apply the following procedure: first, we bin the whole phase-space distribution in bins of size $0.04 \text{ Mpc} \times 50 \text{ km s}^{-1}$. After that, we take all those bins lying in two stripes $4,500 \text{ km s}^{-1} < |v_{\text{los}}| < 6,000 \text{ km s}^{-1}$, where we assume that all the galaxies there belong either to the pure foreground or to the pure background sample. Then, we fit a quadratic polynomial dependent of both v_{los} and r_{\perp} to the points in both stripes, and use the interpolated background model to correct the ‘‘inner’’ phase-space region bins. We use a function that depends not only on r_{\perp} , but also on v_{los} ; this is because at high redshifts, and due to observational selection, we may have more spectroscopic measurements of those galaxies that are closer to us with respect to the BCG (i.e., have a negative v_{los}), than further away (positive v_{los}). The background-corrected phase-space diagrams for the three cluster catalogues can be seen on the right handside of Fig. 6.

In Fig. 6 we can spot two clearly distinguishable regions: the *inner*, dynamically relaxed, region of the cluster at $r_{\perp} < 1.5 - 2$ Mpc, where iso-density contours are closed, and, at larger radius, the *outer* radial infall region, highly compressed along the line of sight. This characteristic trumpet-shaped phase-space distribution is applied as a ‘‘caustic method’’ (Diaferio 1999) related to the escape velocity, to infer cluster mass profiles dynamically, where many redshifts of cluster members can define the caustic location. See Zu & Weinberg (2013) and Lam et al. (2013) for recent developments on the field.

Following the method described in Wojtak et al. (2011), we split the background-corrected phase-space diagram into different transverse distance bins, and measure the velocity distribution within these bins. In order to fit this distribution and measure any possible deviation from $\langle v_{\text{los}} \rangle = 0$, we adopt the double Gaussian function form: $A \exp((v_{\text{los}} - \Delta)^2 / 2\sigma_A^2) + B \exp((v_{\text{los}} - \Delta)^2 / 2\sigma_B^2)$, where both Gaussians, each with different amplitude and variance, share the same mean velocity Δ . We present now the results obtained for each of the catalogues used in our analysis.

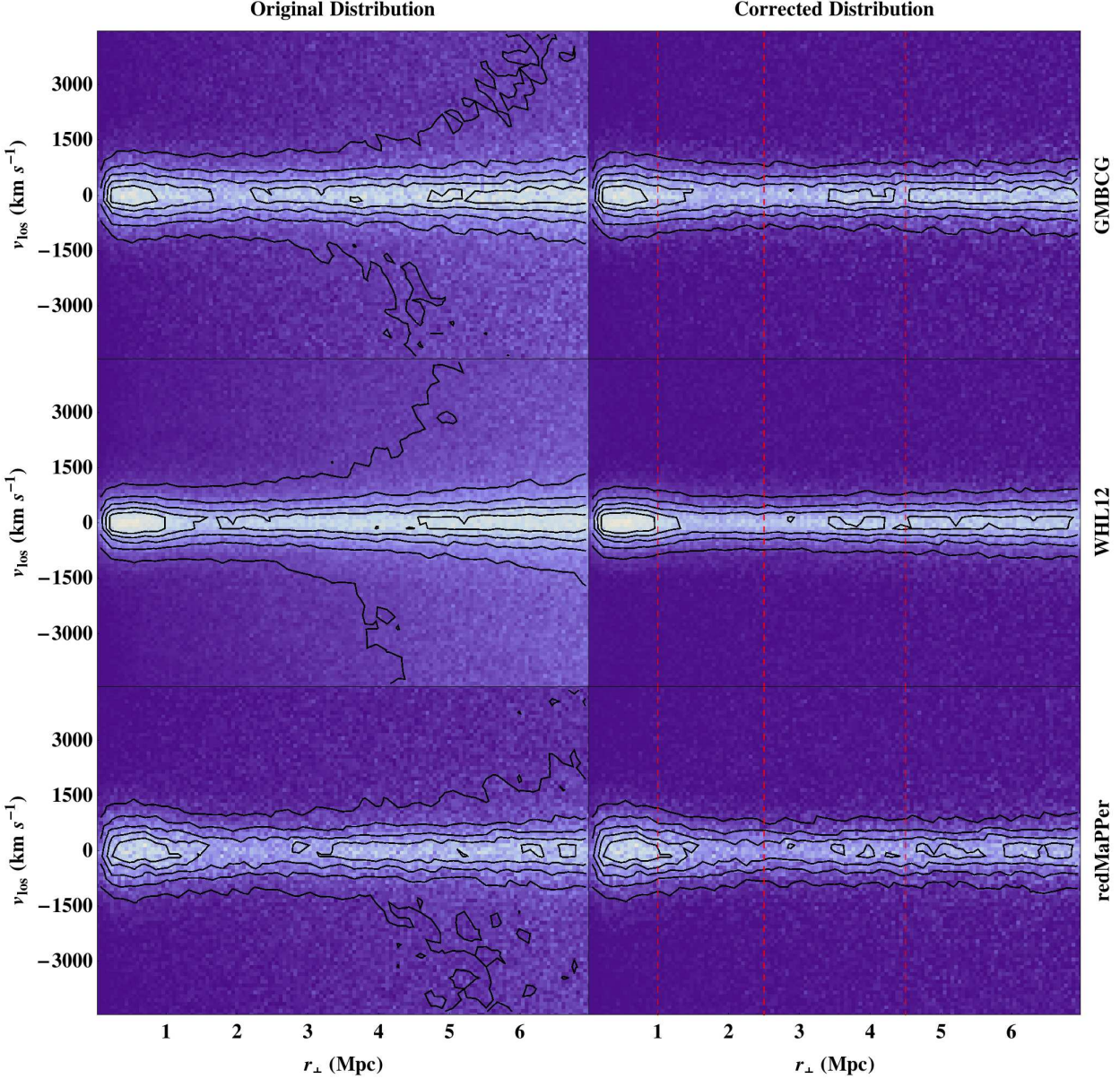


Figure 6. GMBCG (top), WHL12 (middle) and redMaPPer (bottom) phase-space diagrams before (left) and after (right) removing statistically the foreground and background contribution of galaxies. Black contours represent iso-density regions. The asymmetry between the positive and negative v_{los} region can be particularly clearly seen in the redMaPPer case. This difference disappears after the statistical interloper removal. We also plot as red dashed lines the boundaries at 1, 2.5 and 4.5 Mpc that will determine the radial bins we will use in Sec. 3. In these diagrams, the position of the BCG is fixed at $r_{\perp} = 0$ Mpc and $v_{los} = 0$ km s $^{-1}$ by definition, and the density is determined by the number of galaxies with spectroscopic redshift measurements around them.

3.2.1 GMBCG Catalog

In order to work only with the most reliable data, we decide to use only those clusters with 6 or more galaxies with spectroscopic redshift measurement in the previously defined phase-space region (7 Mpc and $\pm 4,500$ km s $^{-1}$), that are located in the redshift range $0.1 < z < 0.4$ (where the catalogue is claimed to be complete), and with a richness greater than 10, which corresponds to $M_{200m} \sim 0.75 \times 10^{14} M_{\odot} h^{-1}$. From the initial 19,867 clusters contained in the spectroscopic catalog, this leaves us with a sample of 4,278 ob-

jects, with mean richness 18 (corresponding to $M_{200m} \sim 1.5 \times 10^{14} M_{\odot} h^{-1}$), and mean redshift $z \approx 0.22$. We display the velocity distribution and the resulting fits in the top part of Fig. 7. The values of Δ obtained from the fits are displayed in Fig. 8. These values are negative for all the radial bins considered, and seem to be consistent with the model proposed when considering all the effects described above, for which the prediction is a nearly flat profile of $\Delta \sim -10$ km s $^{-1}$ at radius beyond $r_{\perp} > 0.5$ Mpc, from the central BCG position. Our measurements are compatible with those obtained

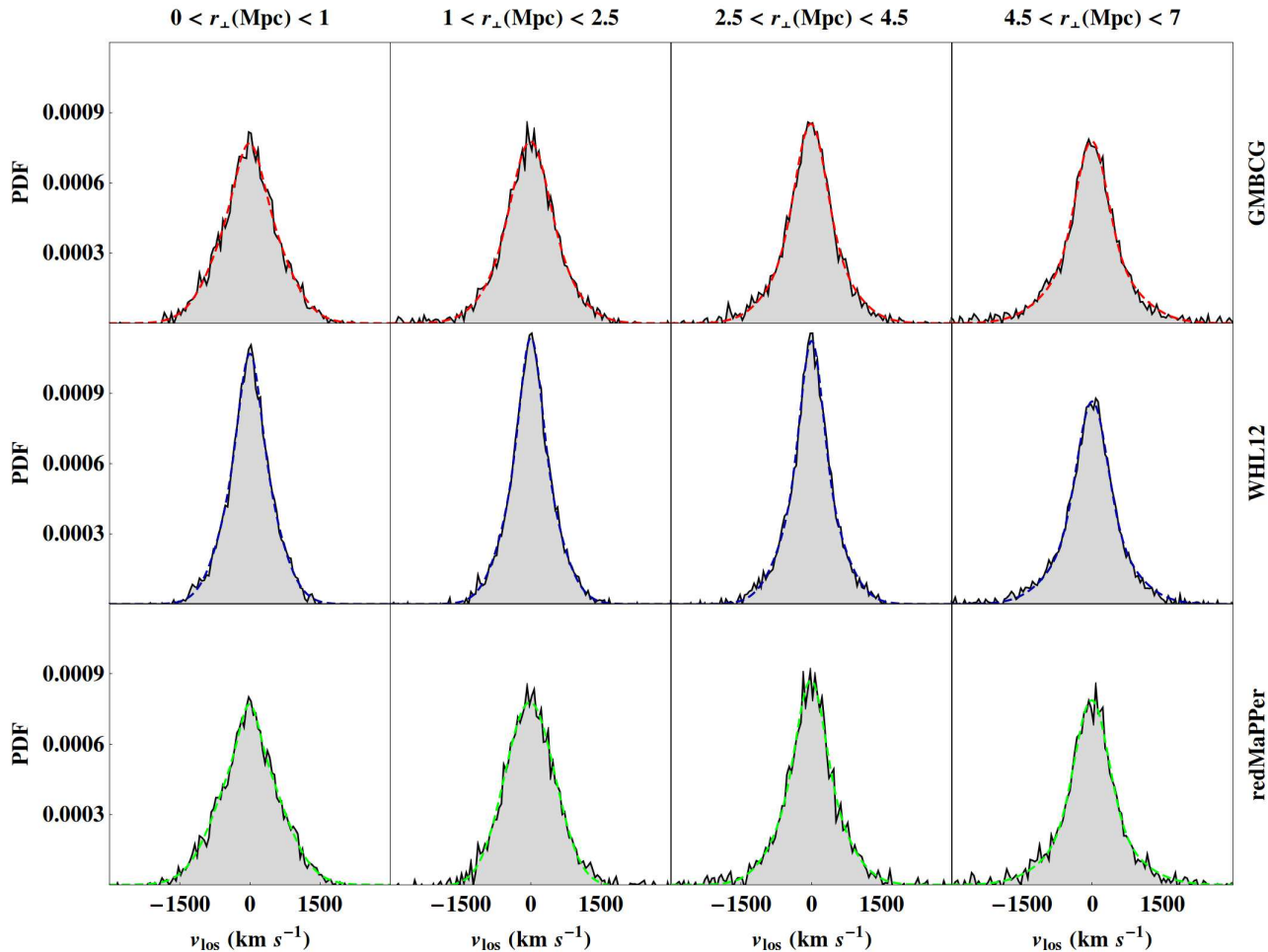


Figure 7. GMBCG (top), WHL12 (middle) and redMaPPer (bottom) velocity distributions for 4 different radial bins, after the background and foreground contribution of galaxies has been removed. In top of these distributions, as dashed curves, the double Gaussian functional fit.

by Wojtak et al., the difference between them coming from the different radial binning used.

We also divide the data into different mass bins in order to test how this measurement may change with cluster mass. As before, we select only those clusters with 6 spectroscopic BCG-galaxy pairs or more. Then, we divide the resulting sample into 3 different mass subsamples. For each of these subsamples we would like to measure the integrated signal up to a certain radius r_{\perp} , but, as we expect cluster size to increase with richness, a galaxy at, say, a distance of 0.5 Mpc from a high richness cluster’s BCG would be deeper in the gravitational potential than a galaxy 0.5 Mpc away from a low richness cluster’s BCG. So, in order to make the measurements more comparable, we convert projected r_{\perp} radial distances from the BCGs into r_{200c} units, i.e., we rescale the comoving transverse distances of the galaxies that belong to a particular cluster using the r_{200c} estimate of that cluster, obtained assuming a NFW halo density profile, and using the concentration-mass relations provided by Bhattacharya et al. (2013), as explained

before in Sec. 2. We then measure, for each of the mass subsamples, the integrated signal of Δ up to $7r_{200c}$, and the resulting values obtained are displayed in Fig. 9. The first and the second mass subsamples, with average masses of $\sim 0.8 \times 10^{14} M_{\odot} h^{-1}$ and $1.4 \times 10^{14} M_{\odot} h^{-1}$, show values of Δ equal to $-11.2 \pm 3.2 \text{ km s}^{-1}$ and $-7.6 \pm 4.0 \text{ km s}^{-1}$, respectively. The third mass subsample, with a higher average mass of $\sim 3.6 \times 10^{14} M_{\odot} h^{-1}$, gives a value of $\Delta = -16.2 \pm 10.8 \text{ km s}^{-1}$. The error in this last measurement is such that it seems inappropriate to claim an observed signal dependence with increasing mass, despite the seemingly detection of a negative internal redshift signal for the three mass subsamples taken together.

3.2.2 WHL12 Catalog

Taking the same conservative approach as above, we discard all those clusters with less than 6 spectroscopic BCG-galaxy pairs in our phase-space defined region. On the other hand, although the WHL12 is claimed to be complete over a

wider cosmological redshift range than GMBCG, we decide to adopt the same limited range as the GMBCG catalogue used above, $0.1 < z < 0.4$, in order to reduce the potential for any systematic differences between both measurements, making tier comparison easier to interpret. These limitations leave us with a sample of 12,661 clusters, with a mean richness of 23 (corresponding to $M_{200m} \sim 1.4 \times 10^{14} M_{\odot} h^{-1}$), and a mean redshift of $z \approx 0.19$. The resulting velocity distribution and fits are displayed in the middle part of Fig. 7 for the 4 different radial bins used, and the fitted values of Δ are shown in Fig. 8. As we can observe from the figure, the measured signal deviates completely from the proposed model: the first and fourth radial bins, centered at 1 Mpc and 5.75 Mpc, show values of Δ consistent with zero. Even worse, the second and third radial bins, centered at 1.75 Mpc and 3.5 Mpc, display positive values of $\Delta \sim +5 \text{ km s}^{-1}$.

The number of clusters contained in the catalogue is large enough as to split it into different mass bins and still have enough number of objects to have a decent signal-to-noise ratio, so we proceed now to do it in order to test the reliability of this detection. In this case we divide those clusters with more than 5 galaxies with spectroscopic redshifts into 5 different mass subsamples. As before, we measure, for each of these mass subsamples, the integrated signal of Δ up to $7r_{200c}$, where here we use the estimation of r_{200c} provided by the WHL12 cluster finder algorithm, a more direct indicator of the size and concentration of each cluster. The resulting values obtained are displayed in Fig. 9. In this case, the results obtained seem to be more illustrative than in the GMBCG case. The Δ value obtained from the first mass subsample, with an average $M_{200m} \sim 0.8 \times 10^{14} M_{\odot} h^{-1}$, seems to be in agreement with the model prediction, but the signal obtained is very weak, compatible with zero at the 2σ level. The second and third mass subsamples, with average masses around 1.1 and $1.6 \times 10^{14} M_{\odot} h^{-1}$, show positive values of Δ . However, the fourth and fifth mass subsamples, whose average masses are $2.4 \times 10^{14} M_{\odot} h^{-1}$ and $4.6 \times 10^{14} M_{\odot} h^{-1}$ respectively, with values of Δ equal to $-17.2 \pm 7.2 \text{ km s}^{-1}$ and $-22.2 \pm 5.4 \text{ km s}^{-1}$, indicate a trend of a larger negative signal for larger cluster masses, corresponding to what one would expect from the model. We may think of this as a result of the cluster finding algorithm being more efficient in the task of identifying real clusters and their corresponding BCG for halo masses above $M_{200m} \sim 2 \times 10^{14} M_{\odot} h^{-1}$, or the noise introduced by substructure and cluster mergers being less important for massive, relaxed clusters. In any case, it is clear that the positive values obtained in the radial global measurement of Δ are explained by the fact that the clusters in the WHL12 catalogue residing in this less massive region dominates over the more massive and “reliable” ones, for the mass distribution shown in Fig. 3 indicates. The difference between GMBCG and WHL12 measurements may reside precisely in the fact that, as GMBCG algorithm is optimized to identify red sequence clusters and WHL12 relies only on galaxy FoF counting for their detection. The former method may contain a higher percentage of concentrated clusters, with a higher degree of virialization resulting in concordance between the measurement of internal redshift effects and the model for which virialization assumed.

3.2.3 redMaPPer Catalog

In the redMaPPer catalog, we also restrict the sample to those clusters in the $0.1 < z < 0.4$ redshift range and with 6 or more galaxies with spectroscopic redshift measurements, reducing the number of useful clusters from 10,197 to only 3,372, these having a mean richness of 35 (corresponding to $M_{200m} \sim 3.2 \times 10^{14} M_{\odot} h^{-1}$, the double than in the two previously considered catalogues), and a mean redshift of $z \approx 0.23$. The velocity distribution with the corresponding fits and the resulting values of Δ obtained from them are shown in Figs. 7 and 8 respectively. Although the amplitude of the signal is expected to be higher for this cluster sample, apart from the second radial bin centered at $r_{\perp} = 1.75$ Mpc, with $\Delta = -16.7 \pm 5.5 \text{ km s}^{-1}$, all the other radial measurements of Δ do not deviate more than $\pm 2 \text{ km s}^{-1}$ from the measurements obtained using the GMBCG catalogue. Even when all the Δ measured points remain negative, there is no clear evidence for a stronger internal redshift signal compared to the one provided by GMBCG catalogue.

Now, as the number of clusters is relatively small, we measure the integrated signal of Δ up to $7r_{200c}$ for only two mass subsamples of clusters. In this case, we use, as in the GMBCG case, the r_{200c} estimates obtained assuming a NFW density profile for the clusters considered. The resulting measurements for the two mass bins, $\Delta = -10.1 \pm 3.5 \text{ km s}^{-1}$ and $-21.1 \pm 5.1 \text{ km s}^{-1}$ at $M_{200m} = 2.4 \times 10^{14} M_{\odot} h^{-1}$ and $5.3 \times 10^{14} M_{\odot} h^{-1}$, respectively, are displayed in Fig. 9. This comparison shows that the measured Δ appears to be more negative for the high-mass sample than for the low-mass one at 1.8σ significance. It is also reassuring that these measurements closely follow the model prediction.

4 REDSHIFT ENHANCEMENT

In this section we describe the measurement of the redshift enhancement of background galaxies behind the SDSS clusters due to lens magnification. This may help elucidate further the results we have found above for the gravitational redshift. We are interested to see to what extent the three cluster samples provide a consistent level of projected mass as determined by a completely independent mass estimate generated by the effect of gravitational lensing.

Lens magnification is caused in this case by a foreground cluster, which acts as a gravitational lens with the lensing shear $\gamma(r)$ and convergence $\kappa(r) = \Sigma(r)/\Sigma_{\text{crit}}$, where $\Sigma(r)$ is the projected mass density of the lens in units of the critical surface density for lensing:

$$\Sigma_{\text{crit}} = \frac{c^2}{4\pi G} \frac{D_s}{D_l D_{ls}}, \quad (13)$$

with D_s , D_l and D_{ls} referring to observer-source, observer-lens and source-lens angular-diameter distances, respectively.

The magnification caused by the lens is given by:

$$\mu = \frac{1}{(1 - \kappa)^2 - |\gamma|^2}, \quad (14)$$

which distorts the background region in two ways: i) as gravitational lensing preserves surface brightness, the flux from a source is amplified as the lens increases the solid angle under

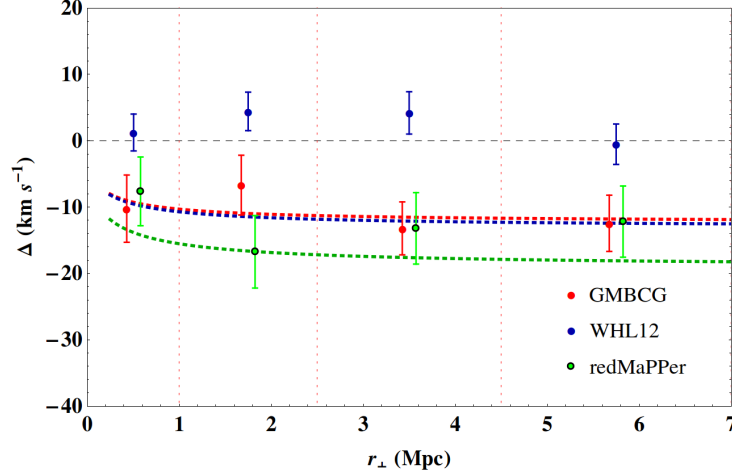


Figure 8. GMBCG (red), WHL12 (blue) and redMaPPer (green) Δ points for 4 different projected radial bins. The r_{\perp} boundaries of these projected radial bins, marked as dashed red vertical lines, are: 0, 1, 2.5, 4.5 and 7 Mpc. Dotted curves represent predictions from model. GMBCG and WHL12 model curves are almost identical, as the mass distribution of the clusters contained in these catalogues is very similar. On the other hand, redMaPPer clusters are, on average, much more massive, leading to an expected stronger effect.

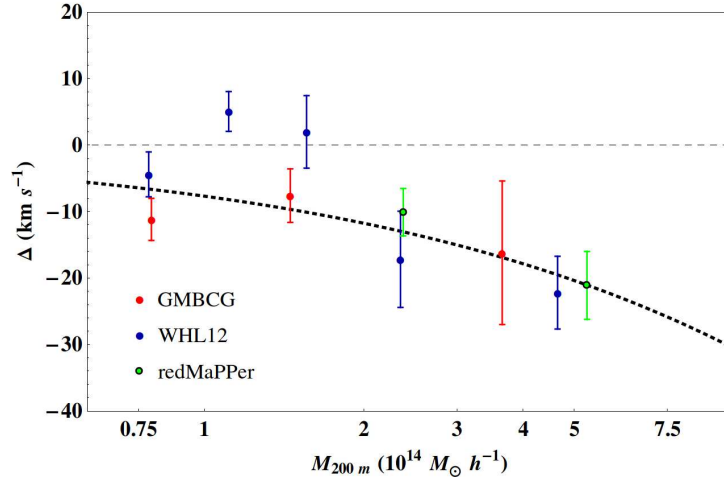


Figure 9. Measurements of the integrated signal of Δ to a distance of $7 r_{200c}$, for 3 different mass bins in the GMBCG cluster sample (red), 5 bins in the WHL12 one (blue), and 2 in the redMaPPer case (green). Dotted curve represents model prediction.

which such source appears. This implies that the luminosity limit of a survey is increased by a factor L_{lim}/μ in the lens region, resulting in a higher surface density of observed background objects due to the ones which could not had been seen otherwise. ii) The sky area behind the foreground lens is expanded, so that the surface density of objects decreases as the effective cross-section behind the clusters becomes smaller. The combination of this two effects and the resulting difference on the number of lensed sourced detected is known as *magnification bias* (Broadhurst, Taylor & Peacock 1995).

Thus, if the observed apparent luminosity of a lensed source is given by $L_{\text{obs}} = \mu L_0$, the observed number of objects with luminosities bigger than L_{lim} is given by:

$$n_{\text{obs}}[> L_{\text{lim}}(z)] = \frac{1}{\mu} n_0[> L_{\text{lim}}(z)/\mu], \quad (15)$$

where the $1/\mu$ factor comes from the dilation of the sky solid angle. Hence, in the case where $n_0[> L(z)] \propto L(z)^{-\beta}$, the previous equation simplifies to:

$$n_{\text{obs}}(z) = \mu^{\beta(z,L)-1} n_0(z), \quad (16)$$

where β is the logarithmic slope of the luminosity function Φ evaluated at L :

$$\beta(z, L) = - \left. \frac{d \ln \Phi(z, L')}{d \ln L'} \right|_L. \quad (17)$$

Taking into account that the number density of objects $n_{\text{obs}}(z)$ depends on redshift, the average redshift of the background lensed sources is given by:

$$\bar{z}_{\text{back}} = \frac{\int n_{\text{obs}}(z) z dz}{\int n_{\text{obs}}(z) dz}, \quad (18)$$

which, if $\beta(z, L)$ is greater than unity, is higher than the average redshift in the absence of gravitational lenses.

4.1 Model

In order to model the expected redshift enhancement signal produced by an ensemble of clusters, we first calculate the effect of magnification on the unlensed redshift distribution $n_0(z)$ of background sources using Eq. (16). To compute the magnification μ as a function of mass and distance from the cluster center, as done throughout the paper (Sec. 2), we adopt the NFW density profile with the concentration-mass relations provided by Bhattacharya et al. (2013), which are favored by recent cluster lensing observations (Okabe et al. 2013; Covone et al. 2014; Umetsu et al. 2014; Merten et al. 2014). We employ the projected NFW functionals given by Wright & Brainerd (2000), which provide a good description of the projected total matter distribution of cluster-sized haloes out to approximately twice the virial radius, beyond which the two-halo term cannot be ignored (Oguri & Hamana 2011; Umetsu et al. 2014). As we shall see, however, this projected NFW model is sufficient to describe the data with the current sensitivity.

As for the luminosity function Φ of the source galaxies, from which we compute the logarithmic slope β (Eq. (17)), we follow CBU13 and use the Schechter parametrization of the V -band luminosity function given by Ilbert et al. (2005), obtained using VIMOS VLT Deep Survey (Le Fèvre et al. 2005) data, and adopt the redshift evolution from Faber et al. (2007): $M_* = -22.27 - 1.23 \times (z - 0.5)$ and $\alpha = -1.35$. The advantage of using this particular survey, although its small 1 deg^2 survey area, resides in that it is much deeper ($0.2 < z < 2.0$, $i < 24$) than the background galaxy sample we are using ($0.45 < z < 0.9$), so that the logarithmic slope of the luminosity function as a function of redshift is very well described in the range of redshift and magnitude we are interested in.

Finally, the limiting luminosity used to evaluate $d \ln \Phi(z, L') / d \ln L'$, is given by:

$$-2.5 \log_{10} L(z) = i_{\text{AB}} - 5 \log_{10} \frac{d_L(z)}{10 \text{ pc}} - K(z), \quad (19)$$

with $i_{\text{AB}} = 19.9$ the limiting magnitude of the BOSS survey, and $K(z)$ the K -correction:

$$K(z) = 2.5 (1 + z) + 2.5 \log_{10} \left(\frac{L(\lambda_e)}{L(\lambda_0)} \right), \quad (20)$$

where the second term can be neglected as the V -band rest-frame flux falls in the i -band at $z \sim 0.5$.

4.2 Experimental Results

Observationally, the redshift enhancement $\delta_z(r)$ of background galaxies is defined as:

$$\delta_z(r) \equiv \frac{\bar{z}(r) - \bar{z}_{\text{total}}}{\bar{z}_{\text{total}}}, \quad (21)$$

where \bar{z}_{total} is the average redshift of the unlensed N_{back} background BOSS galaxies:

$$\bar{z}_{\text{total}} = \frac{1}{N_{\text{back}}} \sum_{i=1}^{N_{\text{back}}} z_i, \quad (22)$$

and $\bar{z}(r)$ the average redshift of the lensed $n(r)$ background galaxies inside a radial bin at a physical distance r from the cluster BCG:

$$\bar{z}(r) = \frac{1}{n(r)} \sum_{i=1}^{n(r)} z_i. \quad (23)$$

A redshift enhancement signal at a significance of 4σ was first detected by CBU13, who used five different cluster catalogues and a total of 316,220 background BOSS galaxies from an earlier data release (DR9). Compared to CBU13, here we use over a factor of two increase in the number of background galaxies (855,097 in total), however we restrict our analysis to those clusters with a BCG spectroscopic redshift to ease the comparison with the gravitational redshift measurements. We note that the more background galaxies somehow compensate the fewer clusters used in the analysis, so that the signal-to-noise ratio is similar to CBU13.

We measure the redshift enhancement signal as a function of radius r from the BCG for the full cluster sample $\delta_z(r)$, and the radially integrated redshift enhancement as a function of mass (assuming a richness-mass relation) $\delta_z(M_{200m})$. We repeat the measurements for each of the three cluster catalogues described in Sec. 2.1.

To estimate the errors on our measurements we generate 500 catalogues with 25,000 random objects each, distributed inside the BOSS angular footprint, and following the same redshift distribution as the cluster catalogue of interest. Then, using the same radial or mass binning, we measure δ_z in the exact same way as for the real background galaxy sample, and define the error bars as the standard deviation of the 500 signals. We also compute the full covariance matrices to account for the re-use of cluster-background galaxy pairs in the stacked signal, when computing the significance. As pointed out in more details by CBU13, here the level of systematic is negligible compared to statistical errors.

4.2.1 Radial Redshift Enhancement

We measure $\delta_z(r)$ in seven logarithmically spaced radial bins in the range $0.04 < r < 15 \text{ Mpc}$. To compare these results with our gravitational redshift results (see Sec. 3), we consider only those clusters for which the BCG has a spectroscopic redshift in the range $0.1 < z < 0.4$. To ensure a significant gap between the cluster lenses and background galaxies and avoid physically associated pairs, we only use the BOSS galaxies with a spectroscopic redshift larger than $z = 0.45$.

We show in Fig. 10 the results obtained for the GM-BCG, WHL12, and redMaPPer cluster catalogues. The model is computed as described in Sec. 4.1, assuming a richness-mass relation for individual cluster and summed over the cluster mass distribution of each cluster sample, as shown in Fig. 3. All measurements feature a $\delta_z(r)$ value in agreement with the models within statistical errors. We note that the difference between the redMaPPer model and the GMBCG/WHL12 models arises from the rather different mass distributions. As seen in Figure 10, the difference is most significant at a scale of $\sim 0.2 - 0.5 \text{ Mpc}$. The detection significance of the redshift enhancement of background BOSS galaxies behind clusters is calculated to be 2.8σ , 4.7σ

and 3.9σ for the GMBCG, WHL12 and redMaPPer cluster catalogues, respectively.

4.2.2 Integrated Redshift Enhancement

To study the mass dependence of this effect, as we have done in Sec. 3, we measure now the radially integrated redshift enhancement signal in different mass bins. To keep an approximately constant signal-to-noise, we divide the GMBCG, WHL12 and redMaPPer cluster samples into 3, 5 and 2 richness bins, respectively. We integrate $\delta_z(r)$ radially in the range $0.04 < r < 0.4$ Mpc, where the signal-to-noise ratio is found to be highest.

Results are displayed in Figure 11. We report a clear tendency of an increasing value of δ_z with increasing average cluster-sample mass, in qualitative agreement with the model. However we observe a $\sim 1 - 2\sigma$ discrepancy at low mass ($M_{200m} < 1 \times 10^{14} M_\odot h^{-1}$) for the GMBCG and WHL12 cluster sub-samples, and a $\sim 2 - 3\sigma$ discrepancy for the WHL12 sub-sample at high mass ($M_{200m} \sim 5 \times 10^{14} M_\odot h^{-1}$).

5 DISCUSSION AND CONCLUSIONS

5.1 Discussion

Using the *Legacy* sample of galaxies, comprising more than 800,000 galaxy spectra, we have detected two independent effects related to the gravitational fields of galaxy clusters identified within this survey. We have produced the phase-space distribution of galaxies around the BCG spectroscopic positions provided by three major cluster catalogues: GMBCG, with 20,119 clusters, WHL12, with 52,682 clusters, and redMaPPer, with 13,128 clusters.

We have then measured the internal redshift distortion Δz associated to each cluster sample as a function of cluster radius. This distortion is identified as the deviation from the BCG velocity of galaxies we associate with these clusters. We have modeled this observational signature for each cluster survey taking into account the combination of the gravitational redshift, the transverse-doppler, the past light cone, and the survey-dependant surface brightness effects. The net gravitational redshift effect that we derive is consistent with the expected cluster richness-mass relation in the case of the GMBCG cluster sample, with values of Δ around -10 km s^{-1} .

In the redMaPPer sample case, with a higher average cluster mass and a lower number of clusters contained in it, the agreement between model and observation is also good within the noise with a difference of at most $\sim +5 \text{ km s}^{-1}$ on average observed above the expectation. In the WHL12 case, we observe an unexpected positive signal ranging from $\sim 0 \text{ km s}^{-1}$ to $\sim +5 \text{ km s}^{-1}$, in complete disagreement with the model based on the richness-mass relation proposed for this sample.

If all our clusters were relaxed, had no sub-structure, and the number of spectroscopic measurements were proportional to the density of galaxies, each cluster would practically follow the stacked cluster distribution of Fig. 6. However, such an ideal case is not realised due to the inevitable level of sub-structure, and from the observational selection

effects and from algorithmic limitations in the definition of clusters and BCG galaxies. Even if BCG finder algorithms were perfect (in the sense of identifying the brightest most massive galaxy of each cluster), it has been shown by Skibba et al. (2011) that the implicit assumption that BCGs reside at the potential minimum is subject to a significant inherent variance leading to a biased measurement of the galaxy velocity dispersion arising from a difference between the measured position of the BCG and the real position of the cluster halo center (Kim & Croft 2004). The underlying offset distribution between the dark matter projected center and the BCGs has been also studied by Zitrin et al. (2012) and Johnston et al. (2007), being shown in the latter that the magnification signal is qualitatively less sensitive to the miscentering effect compared to the shear signal. In principle, stacking all the velocity distributions of galaxies around BCGs into an effective distribution accounts for some of the previously mentioned effects, and enables us to measure any statistical deviation Δ from $\langle v_{\text{gal}} \rangle = 0$. This is what we measured in Sec. 3. However, if we look again at the galaxy velocity distributions (Fig. 7) from which we measured Δ , we see that the velocity distributions obtained from GMBCG, WHL12 and redMaPPer catalogues are different. A further analysis of these velocity distributions shows that this difference holds for different ranges of mass. In the ideal relaxed case, these profiles should follow $\sigma_{\text{obs}}^2 = \sigma_{\text{gal}}^2 + \sigma_{\text{BCG}}^2$, relation from which σ_{gal} is obtained after assuming a relation between the BCG motion and the velocity dispersion of satellite galaxies, $\sigma_{\text{BCG}} = \alpha \sigma_{\text{gal}}$. Wojtak et al. and Zhao et al. consider $\alpha \simeq 0.3$, but it is pointed by Kaiser that the frequent misidentification of BCGs as central galaxies would lead to a higher value of $\alpha \sim 0.5$.

Using the appropriate richness-mass relation for each cluster sample, we analyzed the dependence of the integrated internal redshift signal with mass, observing a clear correlation between the intensity of the signal Δ and the average mass of the sample, especially in the range $M_{200m} > 2 \times 10^{14} M_\odot h^{-1}$, where the measurements follow particularly well the model. The positive radial Δ signal in the WHL12 catalogue seems to mainly arise from lower mass clusters in the range $M_{200m} < 2 \times 10^{14} M_\odot h^{-1}$.

We have also measured the level of magnification bias in each cluster survey, using the latest DR10 BOSS 850,000 galaxy spectra, almost tripling the number of galaxies used in the first measurement of this effect by CBU13. We detect a clear radial redshift enhancement of the background galaxies behind clusters in all three surveys with a significance of 2.8σ , 4.7σ and 3.9σ levels for GMBCG, WHL12 and redMaPPer cluster catalogues respectively.

Making use of the previously employed richness-mass relations, we have also measured the integrated signal out to $r_\perp = 0.4$ Mpc for different subsamples of clusters with different average masses. After modeling this gravitational lensing feature using projected NFW functionals for the clusters and luminosity functions based on deep spectroscopic surveys, we find a generally good agreement between theoretical predictions and observations for the three cluster catalogues, with a clear increase of the mean redshift of background sources at smaller decreasing projected clustercentric radius from the BCG, and also an increasing redshift enhancement with increasing cluster masses. The WHL12 catalogue follows less well the model for the low and the high mass bins

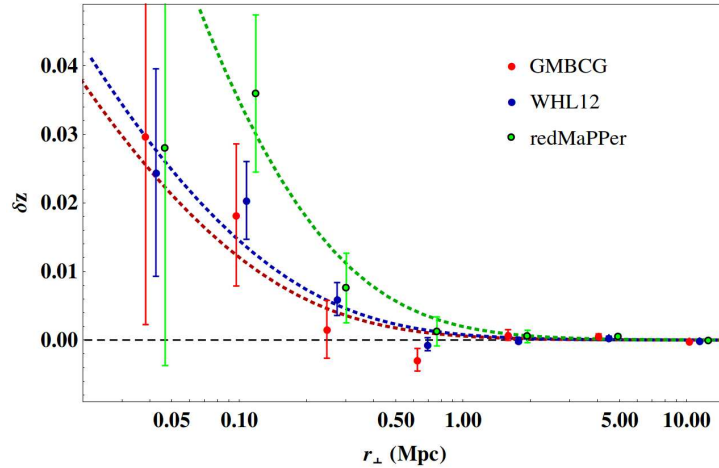


Figure 10. Radial redshift enhancement signals for the GMBCG (red), WHL12 (blue) and redMaPPer (green) cluster catalogues. The dotted curves represent the model predictions for the three different considered cluster samples assuming a richness-mass relation. For visual clarity, the symbols for GMBCG and redMaPPer are horizontally shifted by $\mp 10\%$ with respect to WHL12.

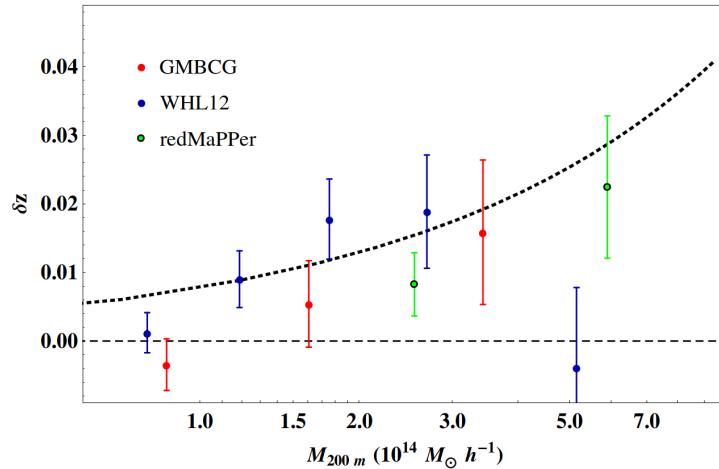


Figure 11. Radially integrated redshift enhancement signal in the range $0.04 < r < 0.4$, in 3 different richness bins in the case of the GMBCG cluster catalogue (red), 5 richness bins in the WHL12 case (blue), and 2 richness bins in the redMaPPer case (green). Model prediction is shown as the dotted black curve.

falling below the expected value, with discrepancies of 2.1σ and 2.5σ , respectively.

5.2 Conclusions

From a comparison of our internal redshift distortion and lensing redshift enhancement measurements for three major cluster samples defined from the SDSS survey, we conclude that the WHL12 catalog, containing the largest number of clusters, is anomalous in the sense that the net internal redshift effect is found to be uniformly positive with radius at a level of $+5 \text{ km s}^{-1}$ instead of negative with $\sim -20 \text{ km s}^{-1}$, as expected given the claimed richnesses of these clusters.

Examining the mass dependence of these results we find it is the clusters with $M_{200m} < 2 \times 10^{14} M_{\odot} h^{-1}$ that introduce the unexpected positive signal, as more massive clusters produce a net redshift of $\sim -20 \text{ km s}^{-1}$, similar to GM-

BCG and redMaPPer samples. Given the much higher number of clusters claimed for the WHL12 sample compared to the other two catalogues, it could be that this positive signal arises from spurious detection of clusters or from chance projection of less massive systems. The internal redshift and lensing magnification signals have totally different sensitivities to line-of-sight projection effects. It is very likely that a higher degree of contamination due to projection effects in this catalogue is responsible for the observed trends in both measurements, as lensing measures the sum of the projected signal.

For the redMaPPer cluster catalogue, which has the smallest sample size due to its conservative minimum richness cutoff, both measurements are shown to agree well with respective predictions albeit the large statistical uncertainties. It also exhibits the best performance in terms of the accuracy of cluster mass estimates because the mass de-

pendence of the signal predicted by models is detected at the 1.8σ level. Our promising measurements of the internal redshift and redshift enhancement effects obtained with the redMaPPer catalogue bode well for future measurements using upcoming large redshift surveys, such as DES, JPAS, eBOSS and EUCLID, which will allow us to define large, clean samples of galaxy clusters using such a robust algorithm.

Our analysis shows that internal redshift measurements are not simply limited by the statistical precision, namely the number of clusters used, but are also sensitive to systematic effects that are not fully understood. In future work, we intend to study these systematics in more detail utilizing phase space information to better account for the inherent velocity dispersion of BCGs with respect to the mean cluster velocity and other possible sources of systematics, such as the effects of cluster miscentering, kinematic behavior of satellite galaxies in relaxed and unrelaxed clusters, and substructures.

Acknowledgements

PJ and TJB thank the ASIAA for generous hospitality. TJB is supported by IKERBASQUE, the Basque Foundation for Science. RL is supported by the Spanish Ministry of Economy and Competitiveness through research projects FIS2010-15492 and Consolider EPI CSD2010-00064, and the University of the Basque Country UPV/EHU under program UFI 11/55. PJ acknowledges financial support from the Basque Government grant BFI-2012-349. TJB, RL and PJ are also supported by the Basque Government through research project GIC12/66. KU acknowledges support from the Ministry of Science and Technology of Taiwan through grants NSC 100-2112-M-001-008-MY3 and MOST 103-2112-M-001-030-MY3.

Funding for SDSS-III has been provided by the Alfred P. Sloan Foundation, the Participating Institutions, the National Science Foundation, and the U.S. Department of Energy Office of Science. The SDSS-III web site is <http://www.sdss3.org/>. SDSS-III is managed by the Astrophysical Research Consortium for the Participating Institutions of the SDSS-III Collaboration including the University of Arizona, the Brazilian Participation Group, Brookhaven National Laboratory, University of Cambridge, Carnegie Mellon University, University of Florida, the French Participation Group, the German Participation Group, Harvard University, the Instituto de Astrofísica de Canarias, the Michigan State/Notre Dame/JINA Participation Group, Johns Hopkins University, Lawrence Berkeley National Laboratory, Max Planck Institute for Astrophysics, Max Planck Institute for Extraterrestrial Physics, New Mexico State University, New York University, Ohio State University, Pennsylvania State University, University of Portsmouth, Princeton University, the Spanish Participation Group, University of Tokyo, University of Utah, Vanderbilt University, University of Virginia, University of Washington, and Yale University.

REFERENCES

Abazajian, K. N., et al., 2009, *ApJS*, 182, 543

- Ahn, C. P., et al., 2014, *ApJS*, 211, 17
 Allen, S. W., et al., 2004, *MNRAS*, 353, 457
 Benitez, N., et al., 2014, arXiv:1403.5237
 Bhattacharya, S., et al., 2013, *ApJ*, 766, 32
 Blanton, M. R., et al., 2003, *ApJ*, 592, 819
 Bonvin, C., Hui, L., Gaztanaga, E., 2014, *PhRvD*, 89, 083535
 Broadhurst, T., Taylor, A. N. & Peacock, J., 1995, *ApJ*, 438, 49
 Broadhurst, T., Scannapieco, E., 2000, *ApJ*, 533, 93
 Broadhurst, T., et al., 2005, *ApJ*, 621, 53
 Cappi, A., 1995, *A&A*, 301, 6
 Coe, D., Umetsu, K., Zitrin, A., et al., 2012, *ApJ*, 757, 22
 Coupon, J., Broadhurst, T., Umetsu, K., 2013, *ApJ*, 772, 65 (CBU13)
 Covone, G., et al., 2014, *ApJ*, 784, 25
 Croft, R. A. C., 2013, *MNRAS*, 434, 3008
 Dawson, K. S., et al., 2013, *AJ*, 145, 10
 Diaferio, A., 1999, *MNRAS*, 309, 610
 Domínguez Romero, M. J. dL., et al., 2012, *MNRAS*, 427, 6
 Dong, F., et al., 2008, *ApJ*, 676, 868
 Eisenstein, D. J., et al., 2001, *AJ*, 122, 2267
 Faber, S. M., et al., 2007, *ApJ*, 665, 265
 Eisenstein, D. J., et al., 2011, *AJ*, 142, 72
 Ford, J., et al., 2012, *ApJ*, 754, 143
 Gronke, M. B., Llinares, C., Mota, D. F., 2014, *A&A*, 562, A9
 Gunn, J. E., et al., 2006, *AJ*, 131, 2332
 Hansen, S. M., et al., 2009, *ApJ*, 699, 1333
 Hao, J., et al., 2010, *ApJS*, 191, 254
 Harrison, I., & Coles, P., 2012, *MNRAS*, 421, 19
 Hildebrandt, H., et al., 2013, *MNRAS*, 429, 3230
 Hu, W., & Kravtsov, A., 2003, *ApJ*, 584, 702
 Huterer, D., et al., 2013, arXiv:1309.5385
 Ilbert, O., et al., 2005, *A&A*, 439, 863
 Jain, B., et al., 2013, arXiv:1309.5389
 Johnston, D. E., et al., 2007, arXiv:0709.1159
 Kaiser, N., 2013, *MNRAS*, 435, 1278
 Kim, Y.-R., & Croft, R.A.C., 2004, *ApJ*, 607, 164
 Koester, B. P., et al., 2007, *AJ*, 660, 239
 Komatsu, E., et al., 2011, *ApJS*, 192, 18
 Lam, T. Y., et al., 2013, *PhRvD*, 88, 3012
 Le Fèvre, O., et al., 2005, *A&A*, 439, 845
 Mantz, A. B., et al., 2014, *MNRAS*, 440, 2077
 Merten, J., et al., 2014, arXiv:1404.1376
 Montero-Dorta, A. D., & Prada, F., 2009, *MNRAS*, 399, 1106
 Navarro, J. F., Frenk, C. S., White, S. D. M., 1997, *ApJ*, 490, 493
 Oguri, M., & Hamana, T., 2011, *MNRAS*, 414, 1851
 Oguri, M., 2014, arXiv:1407.4693
 Okabe, N., et al., 2013, *ApJ*, 769, 350
 Rapetti, D., et al., 2013, *MNRAS*, 432, 973
 Rozo, E., et al., 2009a, *ApJ*, 699, 768
 Rozo, E., et al., 2009b, *ApJ*, 703, 601
 Rykoff, E. S., et al., 2012, *ApJ*, 746, 178
 Rykoff, E. S., et al., 2014, *ApJ*, 785, 104
 Sadeh, I., et al., 2104, arXiv:1410.5262
 Skibba, R. A., et al., 2011, *MNRAS*, 410, 417
 Smee, S. A., et al., 2013, *AJ*, 146, 32
 Strauss, M., et al., 2002, *AJ*, 124, 1819

- Szabo, T., et al., 2011, *AJ*, 736, 21
Takada, M., 2010, *AIPC*, 1279, 120
Taylor, A. N., et al., 1998, *ApJ*, 501, 539
Tempel, A., et al., 2014, *arXiv:1402.1350*
Tinker, J., et al., 2008, *ApJ*, 688, 709
Umetsu, K., et al., 2011, *ApJ*, 729, 127
Umetsu, K., et al., 2012, *ApJ*, 755, 56
Umetsu, K., 2013, *ApJ*, 769, 13
Umetsu, K., et al., 2014, *arXiv:1404.1375*
Watson, W., et al., 2014, *MNRAS*, 437, 3776
Wen, Han & Liu, 2009, *ApJS*, 183, 197
Wen, Han & Liu, 2012, *ApJS*, 199, 34
Wojtak, R., et al., 2007, *A&A*, 466, 437
Wojtak, R., et al., 2011, *Nature*, 477, 567
Wright, C. O., & Brainerd, T. G., 2000, *ApJ*, 534, 34
York, D. G., et al., 2000, *AJ*, 120, 1579
Zhao, H., et al., 2013, *PRD*, 88, 4
Zitrin, A., et al., 2012, *MNRAS*, 426, 2944
Zu, Y., & Weinberg, D. H., 2013, *MNRAS*, 431, 3319
Von der Linden, A., et al., 2014, *arXiv:1208.0597*
Waizmann, J.-C., Ettore, S., Moscardini, L., 2011, *MNRAS*,
418, 456